International Forum on Aeroelasticity and Structural Dynamics
IFASD 2017
25-28 June 2017 Como, Italy

ADJOINT-BASED MESH ADAPTATION FOR DIRECT FLUTTER PREDICTION

Kevin G. Wang[1], Philip S. Beran[2], Shunxiang Cao[3]

[1]Department of Aerospace and Ocean Engineering, Virginia Polytechnic Institute and State University
Blacksburg, VA 24061, USA
kevinwgy@vt.edu

[2]Aerospace Systems Directorate, Air Force Research Laboratory (AFRL/RQVC)
Wright-Patterson AFB, OH 45433 USA
philip.beran@us.af.mil

[3]Department of Aerospace and Ocean Engineering, Virginia Polytechnic Institute and State University
Blacksburg, VA 24061, USA
csxtovt@vt.edu

Keywords: flutter, bifurcation, mesh adaptation, piston theory, adjoint variables

Abstract: Adjoint-based mesh adaptation is applied to the prediction of flutter with a direct, Hopf bifurcation method. Adjoint variables are computed with respect to the objective of flutter speed, and regarded as an *a posteriori* indicator of the relative importance of local conditions to this objective. The magnitude of adjoint variables is then used to drive mesh adaptation for improved accuracy. The methodology is demonstrated on the model problem of a one-dimensional thin panel in supersonic flow. The structure is modeled using the von Kármán plate theory, the fluid pressure distribution on the panel is modeled using piston theory, and the combined system of equations is discretized using a finite difference method. Mesh adaptation is used to take an initially uniform mesh and locally refine it to better resolve parts of the panel that are judged to be relatively more important to flutter prediction. Three mesh-adaptation criteria are compared and contrasted based on: (1) strict adjoint-based mesh adaptation using the adjoint variables, (2) feature-based mesh adaptation using the solution curvature, and (3) a relaxed adjoint-based mesh adaptation using a combination of the adjoint variable and the solution curvature. The results show that for coarse meshes, criteria leveraging adjoints clearly outperform feature-based adaptation for predicting the critical dynamic pressure at flutter onset.

1 INTRODUCTION

The accurate prediction of flutter is of utmost importance in aerospace vehicle design, as the large-amplitude structural oscillations resulting from flutter may precipitate structural failure. Whereas time-domain analysis is the most widely used method for predicting flutter onset in numerical simulations involving Computational Fluid Dynamics (CFD), a direct method based on bifurcation analysis [1–3] is advantageous in several aspects, such as searching over a multi-parameter space [4], accounting for parametric uncertainties in the prediction [5, 6], and computing sensitivities for design optimization [7, 8]. These advantages are gained by the precise manner in which flutter points are computed through a linearized, frequency-domain approach avoiding costly time integration.

Whether flutter onset is computed with direct or time-domain CFD, reliably generating computational meshes suitable for economical analysis is a significant challenge; i.e., confidently forming meshes to meet a computational budget. The authors have not found much literature guiding analysts as to where to cluster mesh points to more accurately predict flutter while bounding computational cost. The critical mode that destabilizes the aeroelastic system may not be more effectively captured by clustering mesh points where an aerodynamicist might cluster mesh points to more accurately predict, say, drag. The critical aeroelastic mode includes structural participation on length scales typically much larger than detailed aerodynamic features. Clustering mesh points to resolve certain detailed features may place too much emphasis on these features than warranted by their impact on the flutter mechanism, and take mesh points away from regions whose integrated impact on flutter is relatively large. Furthermore, a mesh ideal for resolving one mode of flutter may not be as effective for a different flutter mechanism (e.g., wing flutter versus flutter of the aircraft empannage). Uniting mesh adaptation with dynamic aeroelasticity was initially studied by Bhatia and Beran [9] for generalized aerodynamic forces used in flutter analysis, but did not investigate the explicit impact of clustering on flutter. This paper examines a more direct link between mesh distribution and accuracy of flutter prediction.

One of the challenges in mesh adaptation is finding a good criterion for adaptation. The most widely used methods employ featured-based criteria, which employ solution gradients, solution curvature, or pre-selected solution features to determine local mesh resolution. These methods often result in some feature being over-refined while others are not refined enough [10]. On the other hand, adjoint-based mesh adaptation is a promising technique of growing interest. Often regarded as a "goal-oriented" approach, the adjoint-based approach examines the contribution of each element of the computational mesh to the variation of a pre-defined simulation objective. Recently, adjoint-based mesh adaptation was successfully applied to CFD and computational structural mechanics (CSM) analyses in which the simulation objective is a functional of the fluid or structure state variable, respectively [11, 12].

In this work, adjoint-based mesh adaptation is applied to direct flutter prediction by specifying the simulation objective to be the flutter speed. Here, the use of a direct method is critical, since adjoint variables weighting the relationship between local residuals and flutter speed variation can be explicitly computed. The authors are not aware of any previous work considering flutter speed as a basis for mesh adaptation.

2 METHODOLOGY AND PROBLEM FORMULATION

In this section, the basic strategy for directly computing flutter points and forming a system adjoint is outlined. This method is applied to the model problem of a one-dimensional thin panel in supersonic flow, which is described next. Finally, specific techniques for the general approach of mesh adaptation are considered to modify the uniform meshes used for baseline analysis of the panel.

2.1 Direct analysis of flutter points and computation of flutter adjoints

For most aeroelasticity models, the spatially discretized fluid and structural governing equations can be written as a system of N first-order ordinary differential equations (ODEs) of the form

$$\frac{d\mathbf{x}}{dt} = \mathbf{f}(\mathbf{x}; \lambda), \tag{1}$$

where $\mathbf{x} \in \mathbb{R}^N$ denotes the aeroelastic state variable. Let λ be a model parameter of which the critical value at flutter onset, λ^* is of interest. In this context, λ^* is a Hopf bifurcation point of the dynamical system (1), satisfying:

$$\begin{aligned} \mathbf{f}(\mathbf{x}, \lambda) &= 0, & (2)\\ \mathbf{J}(\mathbf{x}, \lambda)\mathbf{p} &= i\omega\mathbf{p}, & (3)\\ \mathbf{q}^T\mathbf{p} - 1 &= 0, & (4) \end{aligned}$$

where $\mathbf{J}$ denotes the Jacobian matrix of $\mathbf{f}$ with respect to $\mathbf{x}$, ω is a real number defining the purely imaginary and critical eigenvalue of $\mathbf{J}$, the critical mode $\mathbf{p} \in \mathbb{C}^N$ is the complex eigenvector corresponding to ω, and $\mathbf{q}$ is a pre-defined normalization vector. The above three equations, governing the flutter condition, can be collectively written as

$$\mathbf{f}_{\text{exp}}(\mathbf{x}_{\text{exp}}) = 0, \tag{5}$$

where $\mathbf{x}_{\text{exp}} = (\mathbf{x}, \mathbf{p}, \lambda, \omega) \in \mathbb{R}^{N+2} \times \mathbb{C}^N$. To obtain the flutter condition, (5) is solved in this work using Newton's method. See [13] for background on Hopf bifurcation analysis, and [8] for details on the direct flutter prediction procedure used herein.

For the purpose of mesh adaptation, the simulation objective is defined as the Hopf bifurcation point λ^*, i.e.

$$I_{\text{obj}} = \lambda^*. \tag{6}$$

If it is momentarily assumed that the sensitivity of λ^* with respect to θ (some arbitrary parameter) is of importance, than this sensitivity can be expressed in terms of the *adjoint variables*, $\mathbf{c}$:

$$\frac{\partial \lambda^*}{\partial \theta} = \mathbf{c}^T \frac{\partial \mathbf{f}_{\text{exp}}}{\partial \theta}, \tag{7}$$

where $\mathbf{c}$ is computed by solving the linear system

$$\left(\frac{\partial \mathbf{f}_{\text{exp}}}{\partial \mathbf{x}_{\text{exp}}}\right)^T \mathbf{c} = \frac{\partial I_{\text{obj}}}{\partial \mathbf{x}_{\text{exp}}} = [\mathbf{0}, \mathbf{0}, 1, 0]^T. \tag{8}$$

Here, the adjoint variables can be thought of as a weighting function for the importance of the local sensitivity of the residual of the expanded bifurcation equations to the flutter point prediction. Where the weighting function, c_i, is large, local changes to the residual are expected to have relatively large influence on λ^*. Thus, $\mathbf{c}$ is used as a function to indicate where mesh refinements are of potentially greatest impact on prediction of λ^*.

It is also noted here that in the Equilibrated Complex Bifurcation (ECB) formulation of [8], the adjoint variables are solved in a manner that condenses out the equilibrium states, such that the adjoint variables are not explicitly associated with the equilibrium states $\mathbf{x}$, but instead are associated with $\mathbf{p}$ and ω. The adjoint variables instead are indirectly influenced by $\mathbf{x}$ through the equilibration process.

2.2 Model problem of supersonic flow over a thin panel

The familiar problem of supersonic flow over a pinned, one-dimensional (1-D) panel of length L and thickness h is considered [14]. See Figure 1. The aerodynamically loaded structure is modeled by the large-deflection, von Kármán plate equation:

$$\frac{\mu}{\lambda}\frac{\partial^4 w}{\partial x^4} - N_x \frac{\partial^2 w}{\partial x^2} + \frac{\partial^2 w}{\partial t^2} = \mu(p_\infty - p) = \mu\left(\frac{1}{\gamma M_\infty^2} - p\right), \tag{9}$$

where the aerodynamic length scales L and freestream velocity, U_∞, are used to place (9) in non-dimensional form [15]. The scaled spatial and temporal coordinates are x and t. The lateral displacement is $w(x,t)$ and is constrained by the boundary conditions $w = \partial^2 w/\partial x^2 = 0$ at the panel end points: $x = 0$ and $x = 1$. Other dimensional and non-dimensional quantities include: the freestream density, ρ_∞; the pressure, p (scaled by $\rho_\infty U_\infty^2$); the ratio of specific heats, γ (1.4); the freestream Mach number, M_∞; the structural density, ρ_s; the mass ratio, $\mu \equiv \rho_\infty L/\rho_s h$. Lastly, λ denotes a non-dimensional dynamic pressure parameter [15]: $\lambda \equiv \rho_\infty U_\infty^2 L^3/D$, where D is the plate stiffness, $D = Eh^3/12(1-\nu^2)$, E is Young's modulus, and ν is Poisson's ratio (0.3). The panel is assumed to be free of structural damping.

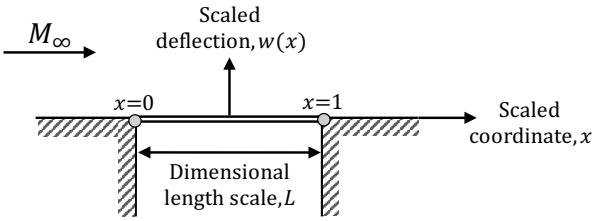

Figure 1: Schematic of a thin, pinned panel in supersonic flow. Pressure loads are applied to the top side of the panel, with no consideration of cavity pressure effects. Pressure loads are computed with piston theory over the unit interval. Adapted from [15].

At dynamic pressures beyond critical, λ^*, (9) becomes dynamically unstable; small perturbations grow until quenched by the nonlinear term $N_x \frac{\partial^2 w}{\partial x^2}$, where the in-plane force N_x grows with panel deflection and decreases with λ [15, 16]:

$$N(x) = \frac{6\mu}{\lambda}\left(\frac{h}{L}\right)^{-2}\left(1-\nu^2\right)\int_0^1 \left(\frac{\partial w}{\partial x}\right)^2 dx \tag{10}$$

The plate is assumed to be subjected to supersonic fluid flow, and the fluid load is modeled using the well-known piston theory:

$$\mu\left(\frac{1}{\gamma M_\infty^2} - p\right) = -\frac{\mu}{\beta}\left(\frac{\partial w}{\partial x} + \left(\frac{M_\infty^2 - 2}{M_\infty^2 - 1}\right)\frac{\partial w}{\partial t}\right). \tag{11}$$

When tightly coupled with the structural equation, the airloads model (11) yields a single, second-order partial differential equation for $w(x)$. On a uniform mesh of N_g grid points, the resulting equation is spatially discretized with second-order-accurate, central-difference approximations at interior points and for the derivative boundary conditions at end points. Implicit handling of ghost points outside the mesh facilitate the construction of the discrete representation. On non-uniform meshes, Taylor-series expansions are used to construct finite-difference approximations using computational stencils equivalent to that employed for uniform meshes. A consequence of retaining the same stencils is the lowering of the formal discretization accuracy to first order on non-uniform meshes.

The spatially discretized equations are placed in state-space form with the definition $\mathbf{x} = [\mathbf{w}, \mathbf{s}]^T$, where $\mathbf{x}$ is the state array, $\mathbf{w} = [w_i]^T$ and $\mathbf{s} = [s_i]^T$ are the arrays of deflections and velocities, respectively. For transient analysis, the equations are integrated in time using the implicit backward Euler scheme using a time step of 0.1 (about 150 time steps per cycle for the cases examined herein). Higher temporal accuracy can be gained with smaller time steps

or improved methods, but were not considered in this study, as the focus of the investigation was not on transient analysis. However, the authors have demonstrated the convergence of the scheme in time, and compared with more accurate methods.

2.3 Mesh adaptation criteria

The mesh adaptation considered in this paper is driven by a discrete distribution function, Q_i, which is used to transform a uniform mesh into a non-uniform mesh characterized by

$$x_{i+1} - x_i = \Delta x_i = \kappa \left(\delta + \frac{1}{Q_i} \right), \quad (i = 1, 2, \ldots, N_g - 1), \tag{12}$$

where $\delta > 0$ is a padding parameter to control the distribution of mesh points, and $\kappa > 0$ is a scaling parameter. A distribution of mesh points is obtained by solving for δ and κ given two constraints:

$$\sum_{i=1}^{N_g - 1} \Delta x_i = 1, \tag{13}$$

$$\max_i \left(\Delta x_i \right) \Big/ \min_i \left(\Delta x_i \right) = \Gamma, \tag{14}$$

where $\Gamma > 1$ is a specified uniformity measure. With constraint (14), the padding parameter is found to be a function of Γ and the extreme values of $\{Q_i\}$:

$$\delta = \left(\frac{1}{\min_i \left(Q_i \right)} - \frac{\Gamma}{\max_i \left(Q_i \right)} \right) \Big/ (\Gamma - 1). \tag{15}$$

Three mesh distribution functions, $Q_i^{(1)}$, $Q_i^{(2)}$, and $Q_i^{(3)}$, are evaluated ($i = 1, 2, \ldots, N_g - 1$):

$$Q_i^{(1)} = \|\mathbf{c}_i\|, \tag{16}$$

$$Q_i^{(2)} = \left\| \left(\frac{\partial^2 P}{\partial x^2} \right)_i \right\|, \tag{17}$$

$$Q_i^{(3)} = Q_i^{(1)} Q_i^{(2)}, \tag{18}$$

$Q_i^{(1)}$ is a strictly adjoint-based distribution function, $Q_i^{(2)}$ is a feature-based distribution function determined from the local curvature of a modal response function P_i (approximated with a central difference formula), and $Q_i^{(3)}$ is a distribution function that combines adjoint and solution features. The modal response function could be evaluated in many ways, but here the following expression was used:

$$P_i = |\mathrm{Re}(w_i)| + |\mathrm{Im}(w_i)| + |\mathrm{Re}(s_i)| + |\mathrm{Im}(s_i)|, \tag{19}$$

where w_i and s_i are the local deflections and velocities at mesh points.

The mesh distribution function can exhibit relatively rapid variations in space whose presence can degrade the accuracy of the model discretization. Generally, smoothing of Q_i is beneficial. This smoothing is accomplished iteratively through the formula

$$\frac{1}{6} \left(Q_{i-1}^{\nu+1} + 4 Q_i^{\nu+1} + Q_{i+1}^{\nu+1} \right) = Q_i^{\nu}, \qquad (i = 1, 2, \ldots, N_g - 1), \tag{20}$$

for J iterates. Here, a symmetric boundary condition is used for the first and last elements.

It should be noted that in this study, it is assumed that the solution and adjoint variables have already been computed on a uniform mesh of equivalent size to the adapted mesh. As a consequence, the adaptation process implemented in this study does not improve the efficiency of the total flutter calculation, but indicates how the mesh should be adapted to achieve a more efficient flutter prediction process. In a more practical context, the selected adaptation criterion would be used to guide coarse-to-fine refinements, where a flutter solution on a fine mesh with a uniform distribution is not computed. Also, a systematic study of modal response functions and smoothing operators different than that described above was not conducted.

3 RESULTS

Results for the flutter of a thin panel in supersonic flow are now presented. First, the consistency is established of values of λ^* predicted by time integration and the direct ECB method, along with comparison of these predictions with data reported in the literature. Then, modal responses and adjoint variables are contrasted, and the implications of these differences on the selected mesh distribution functions are discussed. Lastly, flutter solutions are computed on non-uniform meshes created from the distribution functions, and the accuracy and convergence properties of these different meshes are compared.

3.1 Accuracy of direct method predictions of flutter onset

The accuracy of the prediction of flutter onset is assessed in two ways: the internal consistency of the current formulation between time-domain and bifurcation analysis, and the accuracy of the λ^* prediction in comparison to published literature. For both studies, a fine mesh of 81 points is selected; $\mu = 0.1$, $M_\infty = 1.5$, and $h/L = 0.002$ are specified. Convergence of the bifurcation method for the panel problem on finer meshes is observed by the authors ($\lambda^* \rightarrow 384.3$); the convergence properties of the ECB scheme (for bifurcation points and their sensitivities) are examined in detail for a different problem in [8].

Predictions of λ^* through bifurcation analysis and time-domain analysis are found to be in excellent agreement. As expected, transient responses for values of λ below λ^* are stable and transient responses for values of λ above λ^* are initially unstable and converge to limit cycles if the simulation is carried out for a sufficient duration. The change in stability is shown in Figure 2 for selected values of λ: 300 and 500, along with images of panel behavior within a response cycle. As seen in the literature, panel responses are largest around the $3/4$-chord location, and the panel response for the unstable case converges to a stable limit cycle of small amplitude.

The jump between the least stable aeroelastic response and the least unstable aeroelastic response forms a "bracket" within which λ^* should lie. Numerical experiments reduced the size of the bracket containing λ^* from $[300, 500]$ to $[380, 390]$, a tolerance of less than 3%, and consistent with the value predicted with the direct method.

The value of λ^* computed with the ECB method is also found to be in excellent agreement with the early seminal work by Dowell [14], which employed a modal-based Galerkin method. The comparison was conducted for a higher Mach number, $M_\infty = 10$. For this condition, λ^* predicted with the current approach is 3425; Dowell predicted 3422, a discrepancy of less

than 0.1%, and within plotting and scanning error (note that this comparison accounts for the different definitions of λ used in the two studies).

Lastly, the authors note that subcritical limit-cycles were not observed, consistent with past observations [14]. The variation of supercritical limit cycle amplitudes is discussed in Section 3.3.

3.2 Computation of flutter adjoint variables and mesh distribution functions

The adjoint variable $\mathbf{c}$ and the eigenvector $\mathbf{p}$ at flutter onset are shown in Figure 3. The different behaviors of $\mathbf{c}$ and $\mathbf{p}$ in this example are remarkable. Specifically, $\mathbf{c}$ has larger magnitude, gradient, and curvature within the left half of the spatial domain ($0 < x < 0.5$), while $\mathbf{p}$ exhibits higher magnitude, gradient, and curvature in the right half of the domain ($0.5 < x < 1.0$). The authors speculate that the divergence of the spatial distribution of $\mathbf{c}$ from that of $\mathbf{p}$ is a result of the time-dependent and modal nature of flutter, where physical conditions upstream of a key aeroelastic response play a particularly significant role in the mechanism.

These differences suggest that the panel is a good model problem in the sense that adjoint-based and featured-based adaptation criteria will likely produce significantly different meshes. The authors also note that the time-domain solution of this problem has been examined, and exhibits the same spatial variation as $\mathbf{p}$, which is not surprising given the weakly nonlinear nature of the problem. This similarity suggests that a mesh adapted for flutter will likely produce superior predictions of limit-cycle response in time-domain analysis, as will be explored below.

The three mesh adaptation criteria described in Section 2.3 are now applied to the generation of non-uniform meshes. Distribution functions are computed using a consistent value of the uniformity measure, $\Gamma = 2$, and a consistent number of smoothing iterations, $J = 10$. The

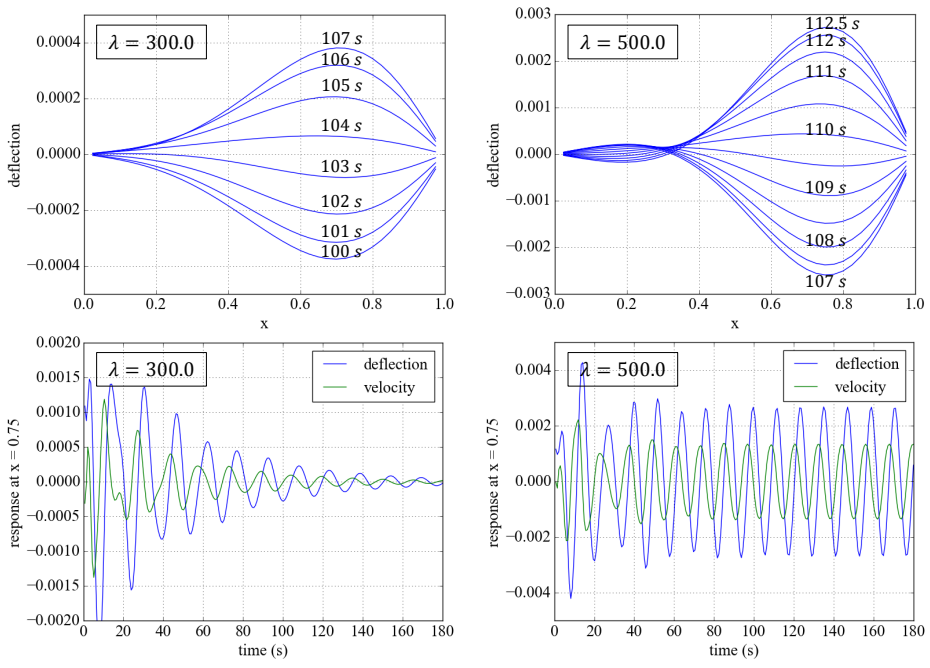

Figure 2: Aeroelastic responses: (left) subcritical stable solution ($\lambda < \lambda^*$) and (right) supercritical limit-cycle oscillation ($\lambda > \lambda^*$) established with time integration.

resulting distribution functions and mesh spacings, after padding and smoothing, are shown in Figure 4 for each of the mesh adaptation criteria assuming a fine mesh of 81 points. At this point, where high values of Q can be visually correlated with small mesh spacing, some properties of the adaptation become clear. For adjoint-based adaptation, the peak in $Q^{(1)}$ is quite large. For curvature-based adaptation, the peak in $Q^{(2)}$ is also relatively large, but not to the extent of the dominance in $Q^{(1)}$. As a consequence, the blended adaptation inherits two dominant peaks in $Q^{(3)}$, with a more substantial rise in the region favored by $Q^{(1)}$.

Figure 5 shows the meshes generated using these criteria for different numbers of mesh points, N_g, assuming $\Gamma = 2$ and $J = 10$ smoothing steps. For $N_g = 41$, it is readily evident that points are clustered in the forward half of the domain for $Q^{(1)}$ owing to adjoint-based weighting, clustered in the trailing half of the domain for $Q^{(2)}$ owing to curvature-based weighting, and then clustered in two regions for $Q^{(3)}$ owing to weighting contributions from curvature and the adjoint variables. For the coarsest grid, $N_g = 11$, the behavior imparted by $Q^{(3)}$ is somewhat different than the other meshes: the mesh is more uniform with some bias in distribution towards the adjoint-based result. The authors attribute this behavior to the relatively large impact of 10 smoothing steps on such a coarse grid. In particular, the strong peak in $Q^{(3)}$ shown in Figure 4 will be smoothed to a larger extent, thereby raising the value of $Q^{(3)}$ near the left boundary with a concomitant decrease in mesh spacing.

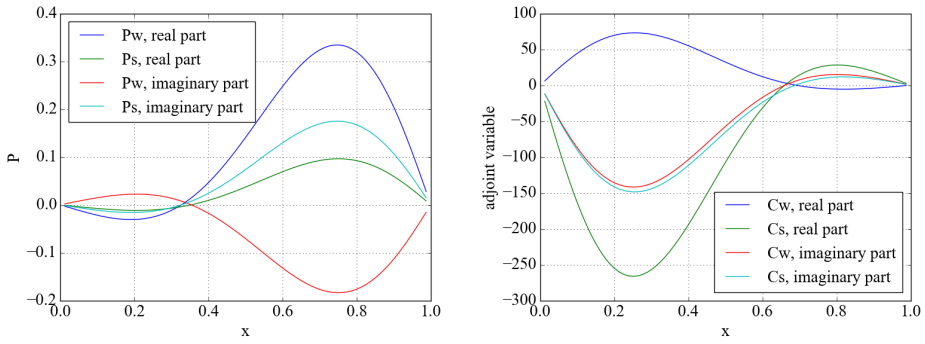

Figure 3: Critical data at flutter: (left) deflection and velocity (real and imaginary) components of $\mathbf{p}$, the neutrally stable eigenvector of $\mathbf{J}$ and (right) similar components of the adjoint variables $\mathbf{c}$.

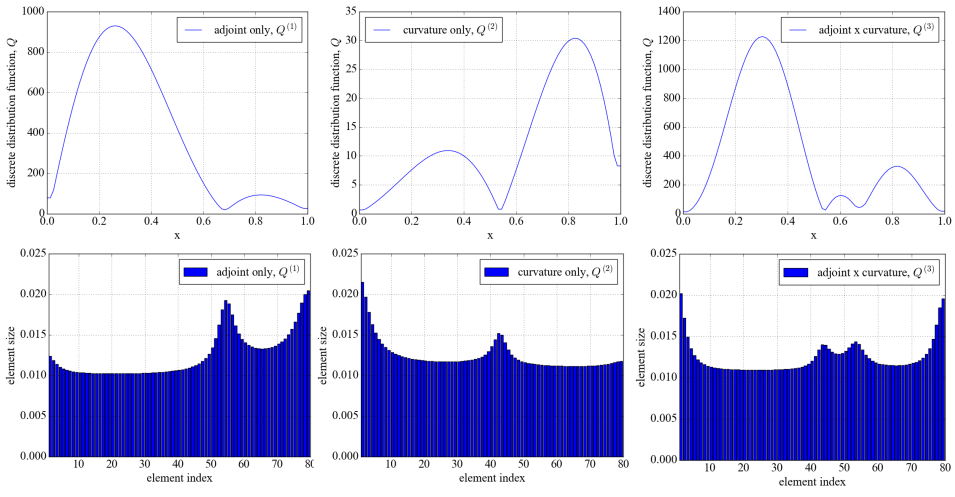

Figure 4: Mesh distribution functions on top row and resulting mesh spacing on bottom row following padding and smoothing for $N_g = 81$: (left) adjoint only, $Q^{(1)}$; (middle) curvature only, $Q^{(2)}$, and (right) adjoint*curvature, $Q^{(3)}$.

3.3 Computation of flutter points and limit-cycle oscillations with non-uniform meshes

The accuracy of computing flutter onset using non-uniform meshes generated with different adaptation criteria is now assessed. To provide an accurate basis for comparison, $\lambda^* = 384.3$ was computed with an overkill mesh of 321 uniformly distributed points. This highly precise result provides an excellent prediction of λ^*_{exact}, the exact point of flutter onset for the panel problem.

In general, adjoint-based adaptation methods ($Q^{(1)}$ and $Q^{(3)}$) outperform the feature-based method ($Q^{(2)}$) in terms of the accuracy of flutter onset prediction for all meshes except the finest, where the results are essentially equivalent. Errors in computed λ^* are plotted in logarithm form in Figure 6 against a measure of average mesh spacing, and for the distribution functions described in Section 3.2. Results are compared to those collected with a uniform mesh, which are seen to converge in a second-order fashion, consistent with the discretization order of accuracy. It is evident that the non-uniform meshes, for which $\Gamma = 2$ is imposed, converge in approximately first-order fashion, again consistent with the discretization approach, but eventually trend in a second-order fashion as more grid points are added. The authors speculate that if second-order accuracy were to be preserved for the analyses conducted with non-uniform meshes, then at least distribution $Q^{(3)}$ would provide higher levels of accuracy than analysis on uniform meshes.

For the coarsest three meshes, the distribution combining adjoint and curvature biases, $Q^{(3)}$, provides the best estimate of λ^*, even out-performing the uniform distribution for the fewest mesh points ($N_g = 11$). As the mesh is refined once, the adjoint-based distributions become as accurate as the uniform mesh, and then lose relative accuracy with further refinement. It is noteworthy that the curvature-only distribution, $Q^{(2)}$, provides the worst results, even though feature-based adaptation is a logical strategy for achieving economy in analysis of steady problems.

Finally, the ability of non-uniform meshes to predict limit cycle amplitudes is assessed. The coarsest mesh is used in this study for two reasons: first, to accelerate the gathering of data, and second, to highlight the differences between predictions obtained with the different mesh distribution strategies. Results are shown in Figure 7. In this figure, the relative inaccuracies in

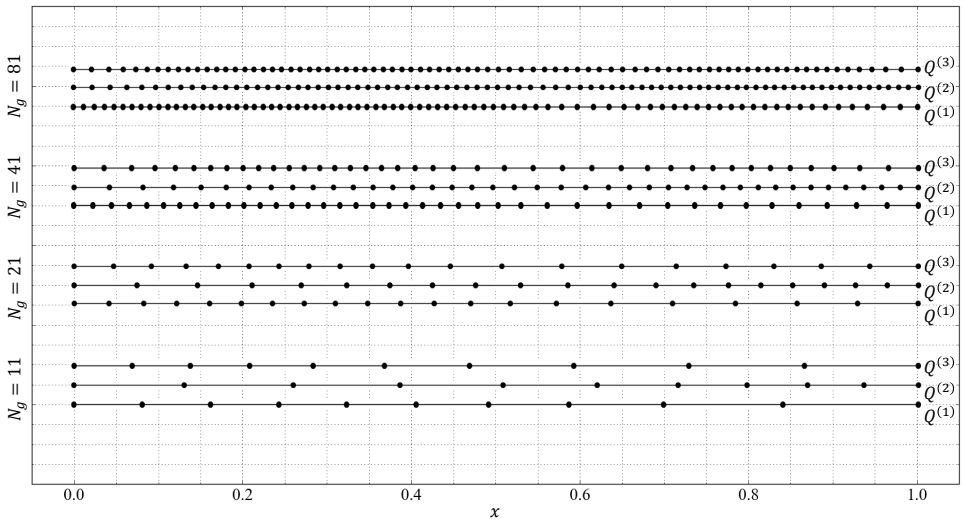

Figure 5: Meshes produced by the three mesh adaptation criteria for different numbers of grid points, N_g.

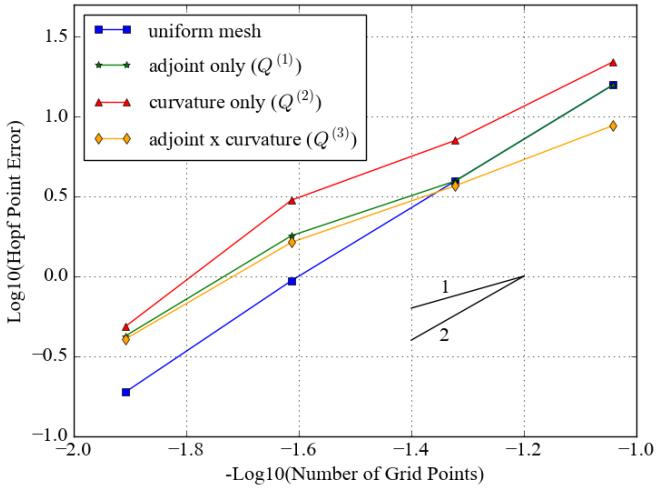

Figure 6: Comparison of error in predicted flutter onset ($\lambda^* - \lambda^*_{\text{exact}}$) as a function of number of mesh points for uniform meshes and the three mesh adaptation criteria: adjoint only, $Q^{(1)}$; curvature only, $Q^{(2)}$; and the product of adjoint and curvature, $Q^{(3)}$ (note that lines of slope 1 and 2 are shown for reference purposes).

the estimations of λ^* are evident and are consistent with findings documented in Figure 6. The most accurate prediction is obtained with the distribution $Q^{(3)}$. It is also clearly seen that limit-cycle amplitudes obtained with the same $Q^{(3)}$ mesh are more accurate than those obtained with the other distribution strategies. For values of λ near the flutter point, the discrepancies in limit-cycle amplitude can be substantial, with the error in amplitude predicted with the $Q^{(3)}$ distribution (curvature-only) approximately doubling the error found with $Q^{(3)}$ (adjoint*curvature).

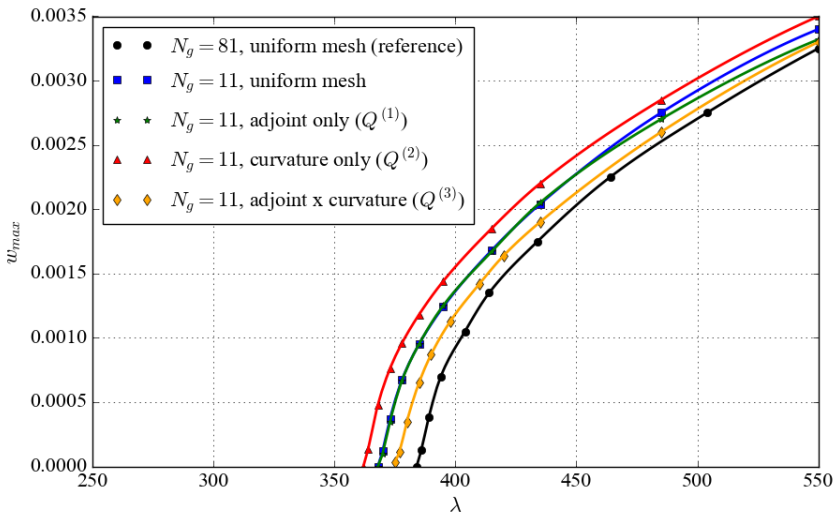

Figure 7: Comparison of limit-cycle amplitudes for the coarsest non-uniform meshes to reference, fine-uniform-mesh solutions. (Limit-cycle amplitudes correspond to $\max(w(x))$ over a full period of oscillation.)

4 CONCLUSIONS

A strategy was developed by which more accurate flutter speeds can be predicted using coarse grids. The approach unifies two ideas. The first idea, explored in a companion paper, led to a quadratically converging process for computing the discrete adjoint solution of the flutter state through a direct approach. The adjoint corresponded to the objective of flutter onset. The second idea, explored in this paper, was to use this flutter-tuned vector of adjoint variables as a basis

for objective-driven mesh adaptation.

For the aeroelastic problem of supersonic flow over a 1-D panel, the strategy is found to be effective for coarse meshes, but dependent on the choice of adaptation strategy. The ability to assess the results is also impaired by the lowering of formal accuracy of the selected discretization scheme for non-uniform meshes. Within this limitation, it is found that a feature-based adaptation driven by solution curvature diminishes accuracy of flutter onset prediction in comparison to uniform meshes. In contrast, adaptation that balances objective-based and feature-based distributions yields increased accuracy on coarse meshes. The reason for this improvement appears to be related to the increased activity of the flutter-tuned adjoint in the forward portion of the panel, an area that would be less important in a feature-based adaptation strategy.

The authors expect the benefits of a mesh adaptation strategy to improve as more realistic problems are tackled, owing to increased dimensionality and the ability to resolve detailed flow features that matter to the determination of flutter speed. The test problem considered herein is very benign in terms of the solution structure, with restricted opportunity for mesh improvement. For general application, however, a more versatile discretization strategy is required to ensure the maintenance of formal accuracy on adapted meshes. The authors also comment that meshes found to be superior for flutter are likely to be superior for conditions near flutter, thus enabling adapted meshes to be recycled for a wider range of simulations, such as for limit-cycle oscillation.

5 ACKNOWLEDGEMENTS

The first author gratefully acknowledges the support of the Air Force Office of Scientific Research (AFOSR) through the 2016 Air Force Summer Faculty Fellowship Program. The second author gratefully acknowledges the support of the AFOSR Computational Mathematics Program administered by Dr. Jean-Luc Cambier (Laboratory Task 17RQCOR473).

6 REFERENCES

[1] Cardani, C. and Mantegazza, P. (1978). Continuation and direct solution of the flutter equation. *Computers & Structures*, 8(2), 185–192. doi:http://dx.doi.org/10.1016/0045-7949(78)90021-4.

[2] Morton, S. A. and Beran, P. S. (1999). Hopf-bifurcation analysis of airfoil flutter at transonic speeds. *Journal of Aircraft*, 36(2), 421–429.

[3] Badcock, K. J., Woodgate, M. A., and Richards, B. (2005). Direct aeroelastic bifurcation analysis of a symmetric wing based on euler equations. *Journal of Aircraft*, 42(3), 731–737.

[4] Beran, P. S. and Morton, S. A. (1997). Continuation method for calculation of transonic airfoil flutter boundaries. *Journal of Guidance, Control, and Dynamics*, 20(6), 1165–1171.

[5] Badcock, K. J., Timme, S., Marques, S., et al. (2011). Transonic aeroelastic simulation for instability searches and uncertainty analysis. *Progress in Aerospace Sciences*, 47(5), 392–423. doi:http://dx.doi.org/10.1016/j.paerosci.2011.05.002.

[6] Beran, P., Stanford, B., and Schrock, C. (2017). Uncertainty quantification in aeroelasticity. *Annual Review of Fluid Mechanics*, 49(1), 361–386. doi:10.1146/annurev-fluid-122414-034441.

[7] Bindolino, G. and Mantegazza, P. (1987). Aeroelastic derivatives as a sensitivity analysis of nonlinear equations. *AIAA Journal*, 25(8), 1145–1146.

[8] Beran, P. S., Stanford, B., and Wang, K. G. (2017). Fast prediction of flutter and flutter sensitivities. Paper 16. International Forum on Aeroelasticity and Structural Dynamics, IFASD 2017, 25-28 June 2017 Como, Italy.

[9] Bhatia, M. and Beran, P. (2015). h-adaptive stabilized finite-element solver for calculation of generalized aerodynamic forces. *AIAA Journal*, 53(3), 554–572. doi: 10.2514/1.J053128.

[10] Roy, C. (2009). *Strategies for Driving Mesh Adaptation in CFD (Invited)*. American Institute of Aeronautics and Astronautics. doi:10.2514/6.2009-1302.

[11] Kouhi, O. E. M. D., M. (2015). Adjoint-based adaptive finite element method for the compressible euler equations using finite calculus. *Aerospace Science and Technology*, 46, 422–435.

[12] Kennedy, G. (2016). *Adjoint-based Mesh Adaptation Techniques for Aggregation Functionals in Structural Design Optimization*. American Institute of Aeronautics and Astronautics. doi:10.2514/6.2016-4127.

[13] Salinger, A. G., Burroughs, E. A., Pawlowski, R. P., et al. (2005). Bifurcation tracking algorithms and software for large scale applications. *International Journal of Bifurcation and Chaos*, 15(03), 1015–1032. doi:10.1142/S0218127405012508.

[14] Dowell, E. H. (1966). Nonlinear oscillations of a fluttering plate. *AIAA Journal*, 4(7), 1267–1275. doi:10.2514/3.3658.

[15] Selvam, R., Visbal, M., and Morton, S. (1998). *Computation of nonlinear viscous panel flutter using a fully-implicit aeroelastic solver*. American Institute of Aeronautics and Astronautics. doi:10.2514/6.1998-1844.

[16] Beran, P., Lucia, D., and Pettit, C. (2004). Reduced-order modelling of limit-cycle oscillation for aeroelastic systems. *Journal of Fluids and Structures*, 19, 575–590.

COPYRIGHT STATEMENT